Open-state structure of veratridine-activated human $Na_V1.7$ reveals the molecular choreography of fast inactivation

Xiao Fan[1,5,6], Jiaofeng Chen[2,5], Lingfeng Xue[3,5], Huan Wang[2], Tong Wu[2], Xiaoshuang Huang[1], Fangzhou Lu[1], Xueqin Jin[2], Chen Song[3,6], Jian Huang[1,6], and Nieng Yan[1,2,4,6]

[1]Institute of Bio-Architecture and Bio-Interactions (IBABI), Shenzhen Medical Academy of Research and Translation (SMART), Guangming District, Shenzhen 518107, Guangdong, China

[2]Beijing Frontier Research Center for Biological Structures, State Key Laboratory of Membrane Biology, Tsinghua-Peking Joint Center for Life Sciences, School of Life Sciences, Tsinghua University, Beijing 100084, China

[3]Center for Quantitative Biology, Academy for Advanced Interdisciplinary Studies, Peking University, Beijing 100871, China

[4]Institute of Chemical Biology (ICB), Shenzhen Bay Laboratory, Guangming District, Shenzhen 518132, Guangdong Province, China

[5]These authors contribute equally.

[6]To whom correspondence should be addressed: Nieng Yan (nyan@tsinghua.edu.cn), Jian Huang (huangjian@smart.org.cn), Chen Song (c.song@pku.edu.cn), and Xiao Fan (xfan@smart.org.cn).

Abstract

Almost all the reported cryo-EM structures of eukaryotic voltage-gated sodium (Na_v) channels, including those of human $Na_v1.1$-$Na_v1.8$, represent various inactivated states that are characteristic of a non-conductive pore domain (PD) surrounded by voltage-sensing domains (VSDs) in varying up conformations. To capture an open-state Na_v structure, we treated purified human $Na_v1.7$ with a natural neurotoxin veratridine (VTD) and solved its cryo-EM structures. Two VTD-bound $Na_v1.7$ complexes were obtained. One, with VTD inserted in the IFM-binding corner (site I), resembles other inactivated structures. The other, wherein VTD traverses the central cavity (site C), represents an activated conformation with the constriction diameter of 8.2 Å at the intracellular gate. Structural analysis reveals the mechanism of action of VTD's bimodal modulation of Na_v channels. More importantly, structural comparison between the open and inactivated states provides advanced molecular insight into the fast inactivation process.

Introduction

In multicellular organisms, electrical signaling is indispensable for nearly all neuronal activities and a wide range of physiological processes [1-3]. Voltage-gated sodium (Na_v) channels govern the initiation and transmission of electrical signals in the form of action potentials in excitable systems such as neurons and muscles. Na_v channels activate upon membrane depolarization, followed by fast inactivation to ensure the repetitive firing of action potentials [1-3]. Following decades of rigorous investigation into their physiological and pathophysiological roles, recent research focus has mainly been on elucidating the structure-function relationship of Na_v channels, as the technological breakthrough in single-particle cryo-electron microscopy (cryo-EM) has led to structural determination of human $Na_v1.1$-$Na_v1.8$ [3-8].

Despite the rapid progress in the structural pursuit of Na_v channels, most of the mammalian Na_v structures captured to date represent inactivated states, characteristic of non-conductive pore domain (PD), depolarized or “up” voltage-sensing domains (VSDs), and the fast inactivation motif, Ile/Phe/Met (IFM), wedged in the receptor site adjacent to the intracellular gate [3]. Towards an in-depth and comprehensive understanding of their working mechanisms, structural snapshots of Na_v channels in all major states are indispensable. As of now, the structure of Na_v channels in the activated or resting state is yet to be determined.

Many strategies have been employed to lock the purified Na_v channels in distinct conformations. Certain peptide toxins successfully trap VSD_{IV} in a down conformation, but the other three VSDs and PD remain unchanged [9,10]. One structure of a rat $Na_v1.5$ mutant $rNa_v1.5$-QQQ, in which the IFM motif was replaced by Gln/Gln/Gln, was described as the open state in the presence of the open-pore blocker propafenone [11]. However, there is a key mismatch between the structural model and the 3D EM reconstruction (Fig. S1). As will be elaborated later, our molecular dynamics simulation (MDS) analysis of the original and corrected structures of $rNa_v1.5$-QQQ suggested that neither could be conductive.

To further probe Na_v gating transitions, we engineered a series of point mutations to modulate the voltage dependence of activation and inactivation of $Na_v1.7$ channels [12,13]. In the structure of $Na_v1.7$M11, a mutant that contains eleven rationally designed single point mutations, VSD_I displays a completely down conformation and the PD is in a tightly contracted state, lacking the fenestrations seen in other inactivated Na_v structures [12]. Electrophysiological characterizations suggest that the structure of $Na_v1.7$M11 may represent a closed-state inactivation (CSI) conformation. The structural study of $Na_v1.7$M11 demonstrates the feasibility of capturing $Na_v1.7$ in distinct functional states. In fact, $Na_v1.7$ has been more extensively characterized structurally than other subtypes, due in part to well-established evidence linking it to pain sensation and subsequent drug development efforts targeting it for analgesic relief [14-17]. Since 2019, more than twenty human $Na_v1.7$ structures

have been determined in complex with diverse modulators [3,12,13,18-23]. $Na_v1.7$ also yields the highest resolution for any Na_v structures, at 2.2 Å for the overall structure[19].

Encouraged by these results, we continued to focus on human $Na_v1.7$ with the goal of determining its structures in both resting and activated states. In an attempt to determine the structure of $Na_v1.7$ in the activated state, we treated the channel with veratridine (VTD), an alkaloid neurotoxin derived from the lily family that is known to act as a potent Na_v opener [24-26]. Here, we report the cryo-EM structures of wild-type (WT) $Na_v1.7$ in distinct VTD-bound conformations. The structure of $Na_v1.7$ with VTD standing near the IFM motif, defined as site I (I for inactivation), is reminiscent of the cannabidiol (CBD)-bound, inactivated state [22]. The other structure, where the elongated steroidal alkaloid VTD traverses the spacious cavity of the PD (site C), appears to represent the activated state with all four VSDs in the up state and a conductive pore. The conductive conformation is verified by MDS analysis. Structural comparison of $Na_v1.7$ in the activated and inactivated states elucidates the dynamic details underlying fast inactivation, and reveals the pathogenic mechanism for dozens of disease-related mutations.

Results

Distinct structures of $Na_v1.7$ treated with VTD

Veratridine (VTD) has long been recognized as a classical sodium channel opener, yet its precise mechanism of action (MOA) remains unclear. We therefore sought to solve the structure of VTD in complex with human $Na_v1.7$. Prior to structural determination, we

validated the functional effects of the purchased VTD. Human $Na_v1.7$ channels, wild type (WT) or mutants, were transiently expressed in HEK293T cells for whole-cell patch-clamp electrophysiological recordings treated with VTD under different conditions.

With standard steady-state activation and inactivation protocols (see Methods), VTD induced a pronounced hyperpolarizing shift in both activation and inactivation curves (Fig. S1 and Tables S1-S4), while concurrently suppressing the peak current amplitude in a dose-dependent manner, with an IC_{50} of 92.7 ± 18.4 μM (Fig. 1A). In parallel, VTD elicited a persistent inward current and a prominent tail current, both of which enhanced with increasing concentrations of VTD (Fig. 1A, *left*). To amplify these small-amplitude currents and probe VTD's use-dependent modulation, we applied a 5-Hz pulse protocol. Upon repetitive depolarizations, VTD produced cumulative peak current inhibition and enhanced tail current induction, yielding an EC_{50} for the tail current of 95.4 ± 16.6 μM (Fig. 1A, *middle and right*). The distinctive bimodal modulation of simultaneous suppression of peak current and induction of persistent and tail currents is consistent with the reported effects of VTD on Na_v channels [27].

For structural determination, we co-expressed human $Na_v1.7$ with auxiliary β1 and β2 subunits and conducted protein purification and cryo-sample preparation following an established workflow [12,18]. Considering the limited solubility, VTD was included throughout the purification process to ensure sufficient channel occupancy. When VTD was applied at

100 μM, three major classes of reconstructions were obtained after cryo-EM data acquisition and processing (Figs. S2 and S3 and Table S5). One class has no density corresponding to the ligand, representing an apo form that is identical to the reported wild-type (WT) structure [12,19] (Fig. S3E). In another class, the density that clearly belongs to a VTD molecule stands next to the IFM motif (Figs. S3D and S4). The overall structure remains similar to the apo channel, with a root-mean-square deviation of 0.96 Å over 1244 Cα atoms in the α subunit when superimposed in PyMOL [28] (Fig. 1B). Local shifts occur in the cytosolic tip of $S6_{III}$ as a result of the insertion of the VTD molecule (Fig. 1B, *right*). Based on our recently proposed definition for ligand binding sites on Na_v and Ca_v channels, this VTD binds to site I (I for inactivation) [21,29]. We refer to this structure as $Na_v1.7V\_I$, which features an inactivated state.

The last class displays marked changes in VTD binding and channel conformation. The elongated VTD molecule traverses the entire central cavity (site C), with its 4,9-epoxycevan and 3,4-dimethoxybenzoate ends pointing to fenestrations I-II and III-IV, respectively (Fig. 1C). We will call this structure $Na_v1.7V\_O$. As will be demonstrated later, the intracellular gate is sufficiently widened in this conformation to conduct Na^+. Unlike CBD, lacosamide, and lamotrigine, each of which simultaneously binds to two sites on the PD [21-23], the pore states in Class I and Class O are different, suggesting exclusive binding of VTD to site I or site C in these two conformations.

One VTD binding pose is similar to that of CBD at site I

The overall structure of $Na_v1.7V\_I$ is similar to the CBD-bound one, with an RMSD of 0.92 Å over 1239 Cα atoms [28] (Figs. 2A and S4A). As aforementioned, two CBD molecules simultaneously bind to the PD of $Na_v1.7$, one inserting into the fenestration (site F) and the other fortifying the IFM binding site by standing next to Ile and Phe [22]. In $Na_v1.7V\_I$, only one VTD is observed in the PD. The 3,4-dimethoxybenzoate moiety of the VTD molecule inserts into the corner enclosed by $S4\text{-}5_{III}$, $S6_{III}$, and $S6_{IV}$, surrounded mostly by hydrophobic residues. The remaining portion of the molecule, containing the cevanine skeleton, protrudes toward the cytosol (Fig. 2A and 2B). This binding pose is compatible with its higher aqueous solubility conferred by several hydroxy groups.

Consistent with the similar binding poses at site I, both VTD and CBD reduce the peak currents and stabilize an inactivated state, the latter manifested by the leftward shift of the voltage-dependence for steady-state inactivation (Fig. S1) [22]. As the MOA of modulators bound to site I has been elaborated in our previous work [22,29,30], we refrain from repeating these details in the current work, but focus on the other binding pose of VTD.

Access of VTD to site C opens the intracellular gate

In $Na_v1.7V\_O$, VTD, along its long axis, is closer to repeats II and III (Fig. 3A, *left panel*). The molecule is coordinated through extensive hydrophobic and polar interactions. $S6_{III}$ engages four residues, Ser1445, Thr1448, Leu1449, and Phe1452, more than any other individual segments (Figs. 3A and S4B). Leu393 and Ile397 on $S6_I$, Leu960 on $S6_{II}$, Trp1332

on $S5_{III}$, and Ile1745 on $S6_{IV}$ contribute to the van der Waals contacts with VTD. The C-terminal residues of the P1 helices in repeat I-III, Thr359, Cys925, and Ala1403, all use their backbone carbonyl oxygen to hydrogen (H)-bonded with the hydroxyl groups of VTD. Phe1405 on the selectivity filter (SF) loop in repeat III also participates in VTD binding (Fig. 3A, *right panels*).

The PD of $Na_v1.7V\_O$ is evidently dilated. Calculation of the radii of the permeation path reveals a constriction site diameter of 8.2 Å, sufficient to permeate a 7.2-Å hydrated Na^+ ion (Fig. 3B). By comparison, the gate for WT apo channel is 5.0 Å (Fig. 3B). Previously, structural study of $rNa_v1.5$-QQQ suggested an open gate (Fig. 3B). However, re-examination of its deposited map (EMD-31519) and structural coordinates (PDB: 7FBS) revealed an error in model building (Fig. S5). An incorrectly assigned π-helix at segment S_I:400-403 induces a positional shift of all the residues downstream of Gly401, resulting in inaccurate analysis of the permeation path (Fig. S5A).

We rebuilt and refined the PD of $rNa_v1.5$-QQQ against the deposited map. The updated coordinates ($rNa_v1.5$-QQQ-rebuilt) substantially improved model fitting to the density map and enhanced model quality metrics across all validation parameters (Fig. S5D). In $rNa_v1.5$-QQQ-rebuilt, the segment S_I:390-429 shows an RMSD of 3.3 Å over 40 Cα atoms compared to the original model, while the rest of the PD remains nearly identical, with an RMSD of 0.4 Å over 542 Cα atoms. The gate diameter of the rebuilt model is 5.6 Å, slightly

smaller than that of the original model, 6.2 Å (Fig. S5E). The rebuilt rNa$_v$1.5-QQQ model will be used for all major comparisons and analyses unless otherwise stated.

HOLE analysis confirms that, among all publicly available Na$_v$ structures, Na$_v$1.7V_O presented in this study is the only one with the gate diameter large enough to potentially allow the permeation of hydrated Na^+ ions. We will present the MDS corroboration of the open pore in the next section. In the following, we examine the mechanism by which VTD dilates the channel.

The two classes of VTD-bound structures can be superimposed with an RMSD of 1.2 Å over 1180 aligned Cα pairs. Despite the prominent structural deviations of the PD segments, most of the VTD-coordinating residues remain nearly unchanged at site C, except those on S6$_{III}$. In particular, Thr1448 and Leu1449 would sterically clash with VTD without a major displacement (Fig. 3C). Of note, Ala substitution of Thr1448 would still need to undergo the conformational changes to avoid the clash between VTD and the Cβ atom. By contrast, replacement of Leu1449 by Ala may avoid the steric clash even when the PD is contracted as in the apo or class I state. Along this line of thinking, Ala substitution of Leu960, a residue on S6$_{II}$ that anchors the other end of VTD, may also provide extra space to accommodate VTD in the absence of major shift of S6$_{III}$.

To test this analysis, we generated $Na_v1.7$ mutants with single-point mutations, L960A, T1448A or L1449A. Whereas T1448A had no significant effect on the bimodal regulation of $Na_v1.7$ by VTD, both L960A and L1449A led to a nearly complete loss of both the persistent and tail currents (Figs 3D and S6 and S7). Meanwhile, these two mutations each rendered $Na_v1.7$ more sensitive to VTD inhibition, which was especially evident in the use-dependent measurement (Figs. 3D-G, and S6). Therefore, Leu960 and Leu1449 appear to be two key residues that couple the site C binding of VTD to pore opening. Interestingly, according to our recently proposed versatile residue numbering scheme for Na_vs [31], these two key residues ($Leu960_{S6II,29}$; $Leu1449_{S6III,29}$) are located at the corresponding positions on $S6_{II}$ and $S6_{III}$, respectively. These results may identify position 29, which is localized around the middle point of the transmembrane segment, to be a key locus on the S6 segments for state switch in Na_v channels.

The gate is conductive in $Na_v1.7V\_O$

In the 3D EM map of $Na_v1.7V\_O$, residues 1465-1497, which correspond to the IFM-containing III-IV linker, are completely invisible. Compared to the IFM-loaded apo $Na_v1.7$ structure, the fenestration on the interface of repeats III and IV is directly connected to the intracellular gate, leaving a wide cleft (Fig. 4A). We performed MDS to examine whether the substantially widened gate is permeable to hydrated Na^+ ions.

The simulations of PDs were conducted under a transmembrane potential of 120 mV. The intracellular gate is fully hydrated in the $Na_v1.7V\_O$ structure. Consistently, ion permeation analysis confirmed the permeation of Na^+ ions with a calculated conductance of 13.8 ± 5.0 pS, which is comparable to the experimental value [32] (Fig. 4D). In contrast, the apo WT $hNa_v1.7$ and the two $rNa_v1.5$-QQQ (original and rebuilt) structures exhibited minimal hydration at the corresponding region (Figs. 4B and 4C). Neither could permeate Na^+ ions in our MDS analysis.

We also characterized the dynamic process of Na^+ permeation through the channel (Fig. 4E). Na^+ ions remained hydrated as they passed through the intracellular gate. Moreover, trajectory analysis showed that permeating ions followed an asymmetric path, with Na^+ ions preferentially located near $S6_{IV}$, as well as the wide cleft between $S6_{III}$ and $S6_{IV}$ (Fig. 4F).

Structural basis for fast inactivation

We previously, in the absence of an open structure, suggested that the IFM motif might execute fast cutoff of the ion flow mainly through pushing $S6_{IV}$ to close the intracellular gate [7,8]. Determination of a conductive structure of $Na_v1.7$ fills up a critical void in the process of fast inactivation and offers an updated view on the cascade of molecular events that complete the fast inactivation in Na_v channels.

When the structures of $Na_v1.7V\_O$ and the apo channel are overlaid, there is nearly no change in their VSDs, all of which exhibit the depolarized or up conformations (Fig. 5A, *left*). By contrast, the S5 and S6 segments and the S4-5 constriction ring in all four repeats undergo structural changes to varying degrees (Fig. 5A, *right*). In all the available Na_v structures, including $Na_v1.7V\_O$, the SF and its supporting P1, P2, and the upper halves of S5 and S6 segments remain rigid (Fig. 5B). We will hereafter refer to this region as the PD shoulder.

Superimposition of $Na_v1.7V\_O$ and the apo structures relative to the shoulder shows tilt of the S6 segments in repeats II-IV, all starting around the fourth helical turn. Note that in repeats I-III, a conserved Gly is positioned on this helical turn, likely representing the key residue that provides the flexibility for the downstream segment (Fig. 5B). At first sight, the cytosolic half of $S6_{III}$ undergoes the most marked displacement, with the Cα atom of the cytosolic tip moving by 8.0 Å; those of $S6_{IV}$ and $S6_{II}$ are displaced by 4.5 Å and 4.3 Å, respectively; $S6_I$ seems to be nearly unchanged (Fig. 5A, *right*). Scrutiny of the structure shows that the fourth helical turn in $S6_I$ undergoes an α→π relaxation from the open to the inactivated state, an important structural shift that reorganizes the inner wall of the pore cavity (Fig. 5B).

Then what are the determinants that lead to the structural re-arrangement of the pore-forming segments? When the IFM motif is accessing the receptor site, the Phe residue, which

would clash with Asn1753 and Ile1756 on $S6_{IV}$, directly pushes Ile1756 toward the $S6_{I}$ segment (Fig. 5C, *upper inset*). Meanwhile, the dragging force exerted by the shift of the III-IV helix, a process that was analyzed by us and others previously [7,10,33], and the van der Waals attraction of Phe1460 on $S6_{III}$ to the Ile and Phe residues in IFM pulls the cytoplasmic terminus of $S6_{III}$ toward $S6_{IV}$.

The displacements of $S6_{III}$ and $S6_{IV}$ have a profound effect on the pore conformation. Concerted pushing of $S6_{IV}$ and pulling of $S6_{III}$ collectively narrows the intracellular gate, making it impermeable to Na^+ ions (Fig. 5A, *right*). The side cleft between $S6_{III}$ and $S6_{IV}$ in the open pore is now stitched by an array of hydrophobic residues, only leaving a small fenestration on the interface of repeats III and IV (Fig. 5D, *left*). On the other side of $S6_{IV}$, the displacement of residues Val1758 and Ile1759 would clash with Ile394 and Leu398 on $S6_{I}$, respectively, if there were no additional conformational changes. The α→π helical transition in the middle turn of $S6_{I}$ affords the solution. The rotation of the ensuing $S6_{I}$ segment turns the bulky hydrophobic chains of Ile394 and Leu398 away, repositioning Ala399 to interact with Ile1759. Another consequence of the α→π shift is to re-orient Phe391 to interact with Tyr1755, further shrinking the volume of the central cavity (Fig. 5D, *right*). The concomitant events accompanying the formation of the IFM binding site and its binding to this site quickly stop ion flow at the narrowed gate.

The above analysis shows that both $S6_{III}$ and $S6_{IV}$ only undergo swing motions, without axial rotation, to close the gate. However, the "apo" channel, like in most other Na_v structures, has a glyco-diosgenin (GDN)-like density penetrating its intracellular gate. We previously analyzed in detail that this conformation, despite having a non-conductive gate, appears to be less ideal for IFM accommodation due to the placement of a polar residue Asn1753 adjacent to the hydrophobic Phe residue from IFM [19] (Fig. 5C, *insets*). We have also observed that the $S6_{IV}$ segment tends to adopt the π form in the presence of channel antagonists, such as Protoxin II (ProTx-II), Huwentoxin IV, and a number of small-molecule inhibitors [19,21-23]. We have analyzed in detail that the simple α→π transition of the single segment $S6_{IV}$ would have multiple consequences, including reshaping the IFM-binding site to a more agreeable hydrophobic cavity, further tightening the intracellular gate to an extent that is too narrow for GDN binding, and closing or narrowing the III-IV and IV-I fenestrations [19].

When the PD structures of $Na_v1.7V\_O$ and the ProTx-II bound $Na_v1.7$ are superimposed relative to the shoulder, the α→π rotation in the middle of $S6_{IV}$ is evident (Fig. 5E, *upper*). Consequently, while the Phe in IFM pushes Asn1753 and Ile1756 away, it also attracts Met1754 to revolve toward the hydrophobic cluster formed by Phe1460, Ile and Phe in the IFM motif (Fig. 5E, *lower*; Movie S1).

Discussion

The structural analyses presented here reveal the molecular foundation for the dual actions of VTD on Na_v channels. Binding to site I stabilizes an inactivated state, consistent with the left shift of the steady-state inactivation curve when the channels are treated with VTD (Fig. S1). Inhibition of the peak currents is likely a collective result of VTD binding to both sites, and site C binding may be responsible for the use-dependence of peak current inhibition as well as the induced persistent currents (Fig. 1A).

The binding pose of VTD at site C is consistent with the reported observation in single-channel recording that VTD led to reduced conductance yet increased open probability of the Na_v channel [34,35]. Channel opening may be induced when VTD is accessing site C. Then, what is the entry site? The use-dependent channel inhibition and opening by VTD, along with the proximity of its 3,4-dimethoxybenzoate end to $S6_{III}$ in both binding poses, suggest that VTD may be initially docked to site I and subsequently travel to site C, a process that opens the intracellular gate. However, we cannot exclude the possibility that VTD may approach the cavity from the fenestrations or the intracellular gate. Addressing this question requires comprehensive characterizations. The static structures reported here set the framework for future computational and experimental analyses.

Uniform or diverse PD conformations in fast inactivation?

Prior to the determination of an open Na_v structure in this study, the PD has mainly displayed three non-conductive conformations among the dozens of eukaryotic Na_v structures, tight,

relaxed, and loose. The PD in Na_vPaS and $Na_v1.7$-M11 represent the most contracted conformation, wherein the diameter of the intracellular gate is less than 2 Å [6,12,36]. This sealed gate cannot accommodate any lipid. In a relaxed PD, exemplified by the "π-form" of the ProTx-II and HWTX-IV bound $Na_v1.7$, the constriction site is less than 3 Å in diameter, still disallowing the penetration of a steroid-like molecule [19]. In the majority of the Na_v structures, the intracellular gate, with a diameter between 5-6 Å, is penetrated with a GDN-like molecule, and we refer to this state as the loose PD (Fig. 6A). Note that three similar states of the PD have been observed in Ca_v channels, although the detailed parameters, such as the gate diameter and the α or π form of the S6 segments, vary [30].

$Na_v1.7$-M11, with its tight PD and one down VSD, may represent the conformation of the closed-state inactivation. Does the tight PD resemble that in the resting channels? To answer this question, a bona fide resting-state structure is necessitated. By contrast, all four VSDs are up in the Na_v structures with relaxed or loose PD [3]. Then, which represents the fast inactivated conformation, the relaxed, the loose, or both? We previously suggested that the relaxed state, in which the chemical environment is more compatible with IFM insertion, may reflect the fast inactivated state. Yet, a key question concerns the steroid-like molecule in the intracellular gate in the loose conformation. If the density is only from a GDN or a cholesterol hemisuccinate, which were supplemented in high concentration during channel purification, such conformation is in essence an artifact. However, is it possible that a cholesterol or steroid molecule may insert into the gate even under physiological conditions?

If so, how quickly can it occur? Is it related to slow inactivation? It is noted that a recent study suggested that fast inactivation might involve rotation of the $S6_{III}$ and $S6_{IV}$ segments. Although no rotation of $S6_{III}$ is observed when the structures of the open and relaxed channels are compared, the $S6_{IV}$ segment does undergo an $\alpha \rightarrow \pi$ transition in addition to the swing motion of the helix. This observation further supports that the relaxed conformation may correspond to the fast inactivated state.

Disease mutations mapped to the inactivation segments

Because fast inactivation in Na_v channels is critical to numerous physiological processes, its mechanism has been studied for decades. Two primary models, the ball-and-chain model[37] and the hinged-lid model[37,38], have been proposed to explain the experimental data. Based on the structural comparison of Na_vPaS and $EeNa_v1.4$, we proposed the "door wedge" model, in which docking of the IFM motif into its receptor site allosterically drives pore closure [6,7]. The study presented here, which reports the long-sought-after structure of an open eukaryotic Na_v channel, provides direct evidence to support the wedge model (Fig. 6B).

In addition, we previously analyzed dozens of disease-associated mutations that are clustered into two mechanistic classes within the context of the wedge model [39,40]. Mutations that weaken IFM-receptor interactions directly compromise the fast inactivation, and those that hinder the conformational coupling required for III-IV linker displacement and pore closure influence the process indirectly (Fig. 6C). Both perturbations would favor channel

opening during prolonged depolarization, resulting in a left shift in steady-state inactivation, enhanced persistent or tail currents, and accelerated recovery from inactivation.

Determination of the open-state structure of $Na_v1.7$ affords the opportunity to further improve our mechanistic understanding of many disease mutations in Na_v channels, in particular with the identification of additional coupling residues, such as those that are involved in the $\alpha\rightarrow\pi$ transitions in $S6_I$ and $S6_{IV}$ during fast inactivation. We will use the generic numbering [31] to describe the representative disease mutations as they may occur in multiple Na_v subtypes. One cluster of mutations resides in the III-IV fenestration, including $Phe_{S6III,40}$, $Met_{S6IV,31}$, $Ile_{S6IV,33}$, and $Ala_{S6IV,34}$, and the other lies in the IV-I fenestration, including $Asn_{S6I,30}$, $Leu_{S6I,33}$, $Tyr_{S6IV,32}$, and $Ile_{S6IV,33}$ (Figure 6C). These positions correspond to pathogenic mutations across multiple Na_v channel subtypes, including $Y1781C/H_{S6IV,32}$, $I1782M/S_{S6IV,33}$, and $A1783T/V_{S6IV,34}$ in $Na_v1.1$-related Dravet syndrome (DRVT), $N406K/S_{S6I,30}$, $L409V_{S6I,33}$, $F1473C_{S6III,40}$, $M1766L_{S6IV,31}$, $Y1767C_{S6IV,32}$, and $I1768V_{S6IV,33}$ in $Na_v1.5$-associated long QT syndrome 3 (LQT3), $L407F_{S6I,33}$ in $Na_v1.6$-linked developmental and epileptic encephalopathy 13 (DEE13), and $N395K_{S6I,30}$ and $F1460V_{S6III,40}$ in $Na_v1.7$-related primary erythermalgia. LQT3 mutations such as $Y1767C_{S6IV,32}$ and $N406K_{S6I,30}$ promote elevated late $I_{Na,}$ and all these mutations accelerate recovery from inactivation compared with WT channels, suggesting destabilization of the inactivated state [41-44].

In sum, the structures of VTD-bound $Na_v1.7$ reveal the molecular basis for the dual modulations of $Na_v1.7$ by this small molecule neurotoxin. The open-state structure of VTD-potentiated $Na_v1.7$ fills an important void in the structural biology of Na_v channels and establishes the framework for detailed understanding of channel gating and fast inactivation.

Acknowledgements

We thank the cryo-EM facility at Princeton Imaging and Analysis Centre for technical support. This work was funded by the National Natural Science Foundation of China (32271252 to N.Y. and 32501081 to J.H.). N.Y. was supported by the Shirley M. Tilghman endowed professorship from Princeton University from 2017 to 2022. X.F. has been supported by the HFSP long-term fellowship (LT000754/2020-L) from the International Human Frontier Science Program Organization (HFSPO) from 2020 to 2023. J.H. and X.F. are supported by the start-up funding from Shenzhen Medical Academy of Research and Translation (SMART).

Author Contributions

N.Y., J.H., and X.F. conceived the project. X.F., J.C., L.X., H.W., T.W., X.H., F.L., X.J., C.S., J.H., and N.Y. designed experiments; X.F. and J.H. performed all experiments related to cryo-EM studies, including protein expression, purification, and 3D reconstructions; J.C. carried out experiments related to electrophysiology; L.X. performed molecular dynamics simulations; X.H. and F.L. prepared the mutant plasmids; X.F., J.C., L.X., H.W., T.W., X.H., F.L., X.J., C.S., J.H., and N.Y. discussed and analyzed data; X.F., J.H., and N.Y. wrote the manuscript with input from all authors. All authors approved the final manuscript.

Competing interests

The authors declare no competing interests.

Figure Legends

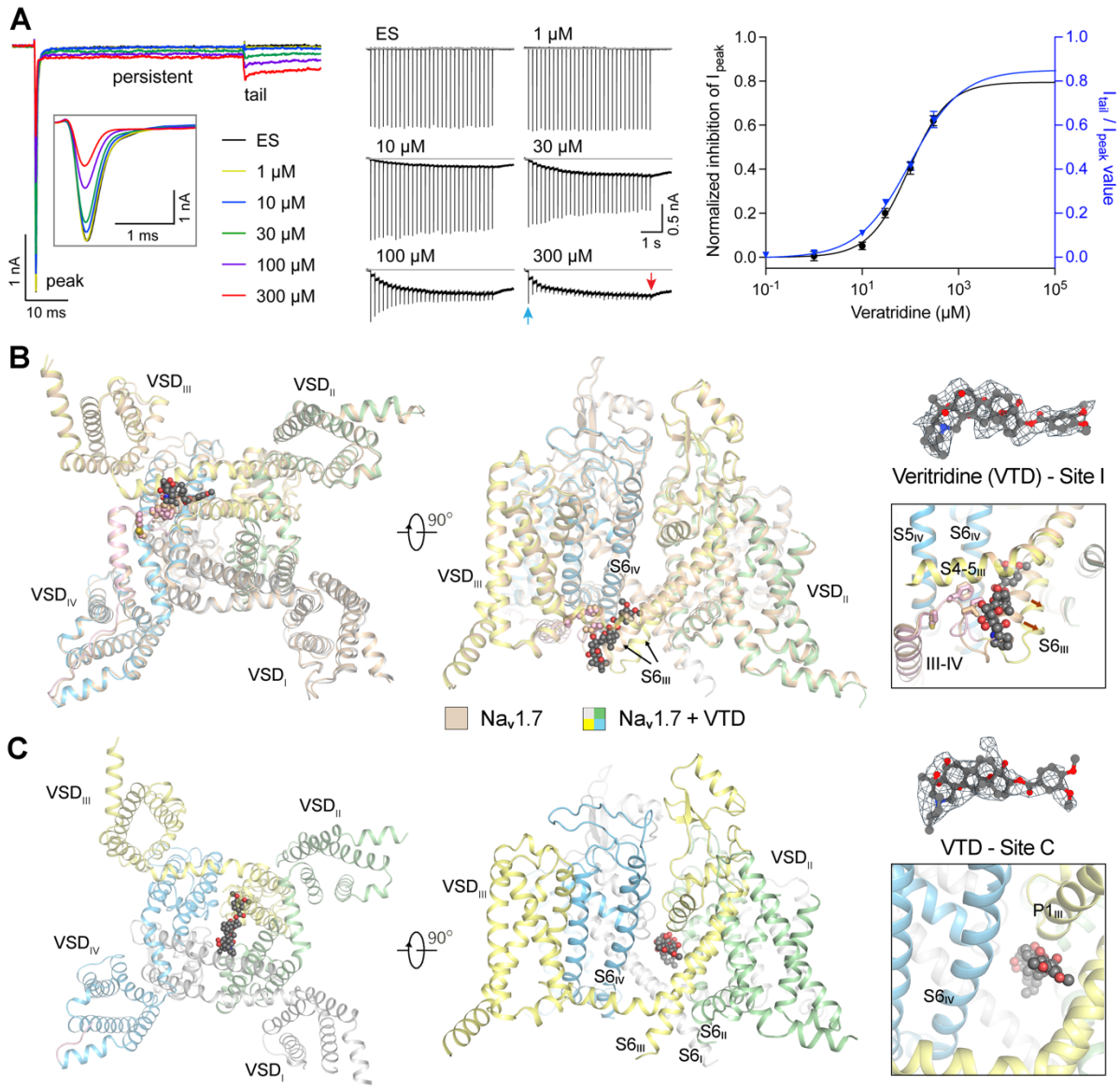

Figure 1 | Bimodal regulation of $Na_v1.7$ by veratridine may be explained by the dual binding poses on the pore domain. (**A**) Use-dependent inhibition of $Na_v1.7$ peak current and enhancement of its tail current by veratridine (VTD). *Left*: Representative traces showing the effects of indicated concentrations of VTD on $Na_v1.7$ peak, persistent, and tail currents. Cells were held at –120 mV and depolarized to a test pulse to 0 mV for 50 ms. An enlarged view of the peak current is shown in the inset. ES, external solution. *Middle*: Representative traces illustrating the use-dependent modulation of VTD on $Na_v1.7$ currents, evoked by a 5-

Hz train stimulation (30 pulses of 5-ms duration from –120 mV to 0 mV). The accumulated tail current (red arrow) was measured and normalized to the amplitude of the first peak current (blue arrow), with both values corrected against the baseline (grey line). *Right*: Concentration-response relationships for VTD-mediated inhibition of $Na_v1.7$ peak current (black curve, IC_{50} = 92.66 ± 18.41 μM, n = 13, 17, 16, 15 ,15) and enhancement of the accumulated tail current (blue curve, EC_{50} = 95.44 ± 16.62 μM, n = 18, 10, 12, 13 ,13, 11). Data are presented as mean ± SEM. Details are presented in Methods and Tables S1-S4. (**B-C**) Three classes of $Na_v1.7$ cryo-EM structures were obtained when treated with 100 μM VTD, including apo and two binding poses for VTD. (**B**) The $Na_v1.7$V_I structure, in which a VTD binds next to the fast inactivation Ile/Phe/Met (IFM) motif, shares a largely similar conformation with the apo channel. We have named this ligand binding site on Na_v channels the site I. Structures of $Na_v1.7$V_I (colored by repeats) and the apo channel (colored wheat) can be superimposed with the root-mean-square deviation (RMSD) of 0.96 Å over 1244 Cα pairs. The major local shift near site I is highlighted by red arrows in the inset. (**C**) In class O, a VTD traverses the central cavity (site C). The VTD densities, shown as grey meshes in ChimeraX [45], are contoured at 6 σ. All structure figures, if not otherwise indicated, were prepared in PyMOL [28].

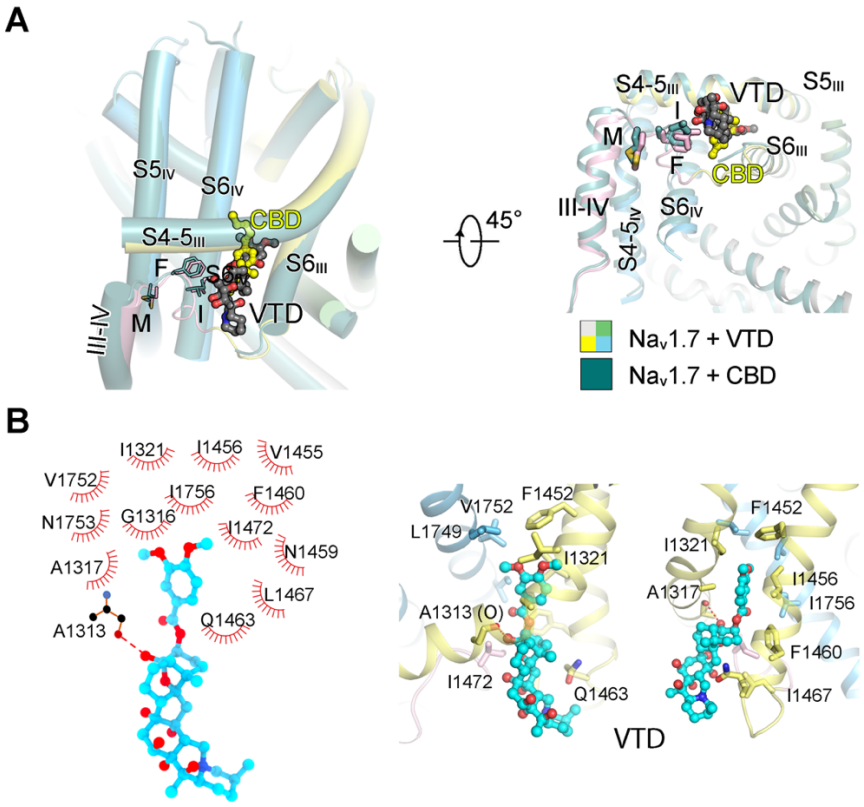

Figure 2 | Site I binding contributes to VTD's antagonistic effect on Na_v channels. (**A**) Similar binding poses of VTD and cannabidiol (CBD) at site I. The structure of $Na_v1.7V\_I$ can be superimposed to the CBD-bound one with an RMSD of 0.92 Å across all 1239 Cα pairs. A tilted side view and a bottom view of their superimposed pore domain are shown. The IFM motif is shown as sticks. The PDB code for CBD-bound $Na_v1.7$ is 8G1A. (**B**) Coordinating details of VTD at site I. The potential hydrogen bonds are indicated with red dashed lines. *Left*: A schematic illustration of the binding details of VTD at site I. *Middle* and *right*: Two side views of VTD coordination. VTD is shown as cyan ball and sticks, and surrounding residues are shown as sticks.

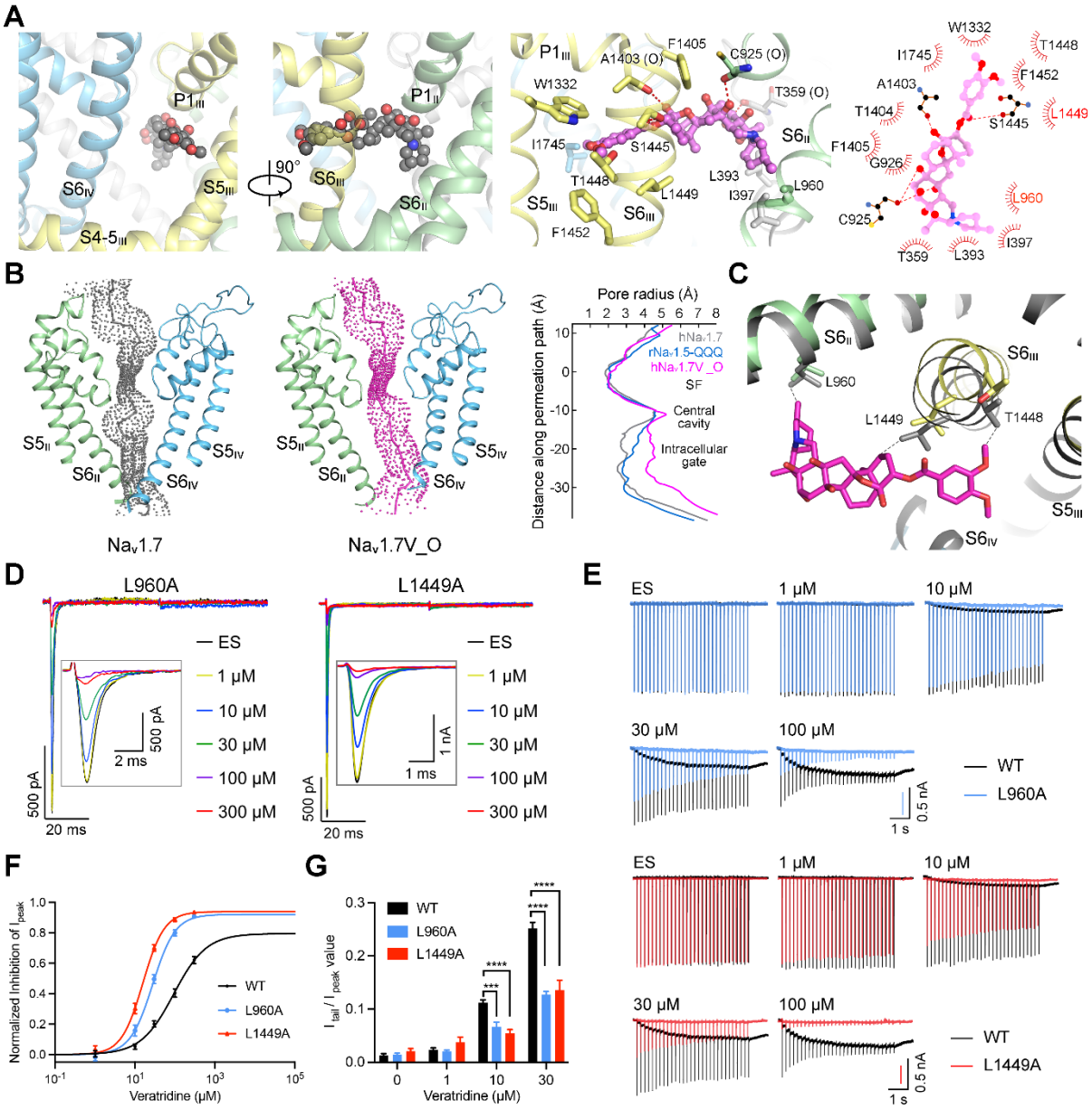

Figure 3 | VTD binding at site C opens the pore. (**A**) Coordination of VTD in the central cavity. *Left two panels*: Two perpendicular views, in addition to that in Fig. 1c, to illustrate the binding pose of VTD at site C. *Right two panels*: Details of VTD binding. Coordinating residues are shown as sticks. (**B**) The pore is substantially dilated in the presence of VTD at site C. The permeation path of the pore domain (VTD omitted) is calculated using HOLE [46]. The radii of the permeation path in the indicated structures are shown on the right. The original error in the model building of the reported structure rNav1.5-QQQ [11] and the

correction are described in Fig. S5. (**C**) The $S6_{III}$ segment appears to play a major role in coupling VTD binding to pore opening. VTD would clash with Thr1448 and Leu1449 if $S6_{III}$ had not shifted outward substantially. The black, dashed lines indicate potential clashes between VTD groups and the two residues. **(D-G)** Functional validation of the structural analysis. Two single point mutations, L960A and L1449A, enhance VTD-mediated inhibition, and nearly abolish its pore opening effect on $Na_v1.7$. (**D**) Shown here are representative traces for the measurement of VTD on $Na_v1.7$-L960A (*left*) and $Na_v1.7$-L1449A (*right*) currents. The protocol is the same as for the WT channel. Cells were held at –120 mV and depolarized to a test pulse to 0 mV for 50 ms. An enlarged view of the peak current is shown in the inset. (**E**) Representative traces illustrating the use-dependent modulation of VTD on $Na_v1.7$- L960A (*top*, blue) and $Na_v1.7$- L1449A (*bottom*, red) compared to $Na_v1.7$-WT (black) currents, evoked by a 5-Hz train stimulation (30 pulses of 5-ms duration from –120 mV to 0 mV). The currents for $Na_v1.7$-WT are the same as in Fig. 1A. (**F**) Concentration-response relationships for VTD-mediated peak current inhibition of $Na_v1.7$-L960A and $Na_v1.7$-L1449A compared to $Na_v1.7$-WT. IC_{50} = 92.66 ± 18.41 μM, n = 13, 17, 16, 15, 15 for $Na_v1.7$-WT; IC_{50} = 27.56 ± 2.30 μM, n = 10, 10, 11, 10, 7 for $Na_v1.7$-L960A; IC_{50} = 15.68 ± 0.97 μM, n = 9, 10, 10, 8, 8 for $Na_v1.7$- L1449A. (**G**) Quantitative analysis of accumulated tail currents normalized to the first peak current of the train stimulation for $Na_v1.7$- L960A, $Na_v1.7$- L1449A and $Na_v1.7$-WT. Data were analyzed by one-way ANOVA; *** $p < 0.001$, **** $p < 0.0001$. Experimental details are presented in Methods and Tables S1-S4.

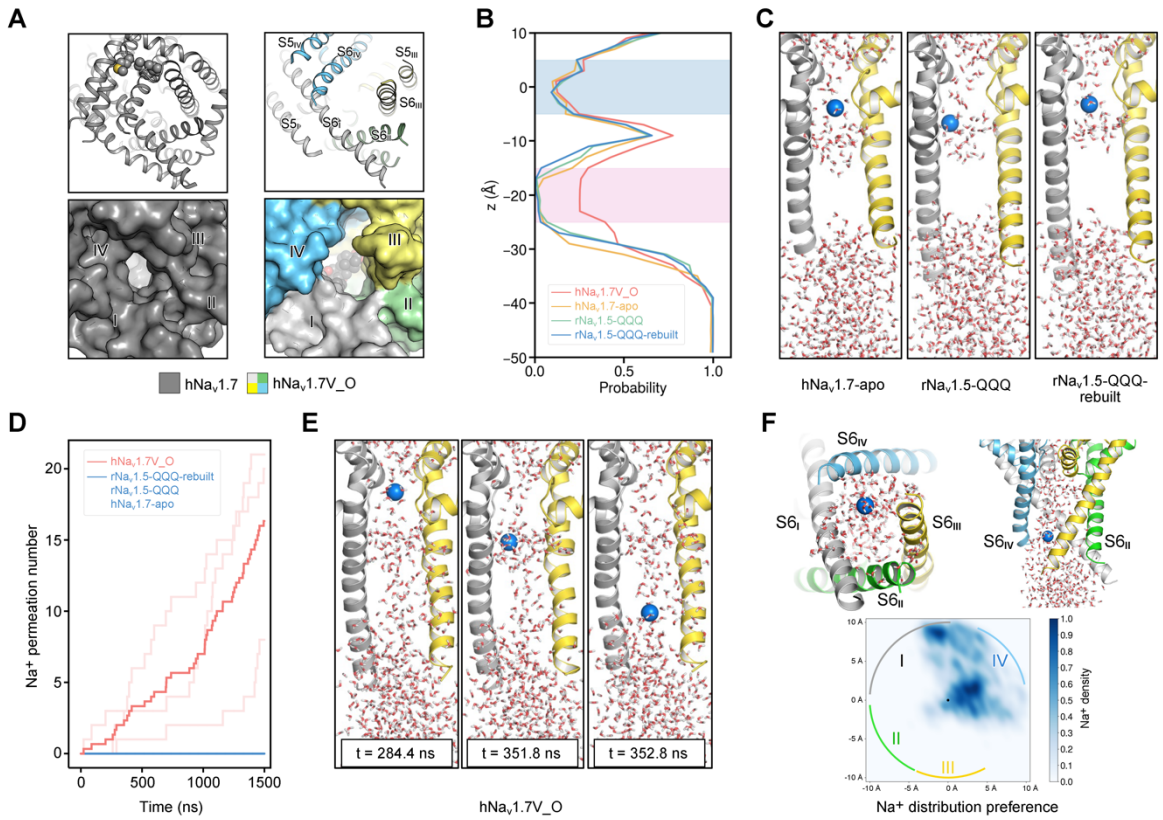

Figure 4 | MD simulation analyses confirm the conductive state of Na$_v$1.7V_O. (**A**) A cleft along the interface of S6$_{III}$ and S6$_{IV}$ is contiguous with the intracellular gate in Na$_v$1.7V_O. Shown here are identical intracellular views of the PD in the apo and class O structures. Cartoon and surface presentations of identical views are shown on the top and bottom, respectively. (**B**) Density distribution of water molecules along the z-axis within the central pore of indicated channel structures. Results are shown for hNa$_v$1.7V_O (red), hNa$_v$1.7 apo (orange), rNa$_v$1.5-QQQ (green), and rNa$_v$1.5-QQQ-rebuilt (blue). Selectivity filter and intracellular gate regions are shaded in blue and pink, respectively. (**C**) Molecular visualization of the hydration state of different channels. For visual clarity, only repeat I and repeat III in the PD are displayed. Sodium ions are depicted as blue spheres, and water molecules are shown as red-and-white sticks. (**D**) Representative ion permeation events in

our MD simulation analysis of the indicated channel structures. The three light red lines represent three independent simulations of the hNa$_v$1.7V_O structure, and the dark red line represents the averaged result. As not a single ion permeation event was observed in any of the three replicate simulations for apo Na$_v$1.7, the original or corrected rNa$_v$1.5-QQQ, the corresponding curves are merged and appear as one single blue line. (**E**) Sequential snapshots of a representative ion permeation event through hNav1.7V_O. The simulation timestamps are indicated in each panel. (**F**) Off-axis ion permeation path. *Top*: A representative snapshot illustrating the angular preference of Na^+ ions as they permeate through the intracellular gate of the hNa$_v$1.7V_O structure. A bottom and a side view of the same snapshot are shown. *Bottom*: Projected two-dimensional distribution of Na^+ ions around the S6 gate to the membrane plane. The shaded areas indicate the S6 regions of repeats I-IV, which are colored gray, green, yellow, and blue, respectively. Also see Methods for details.

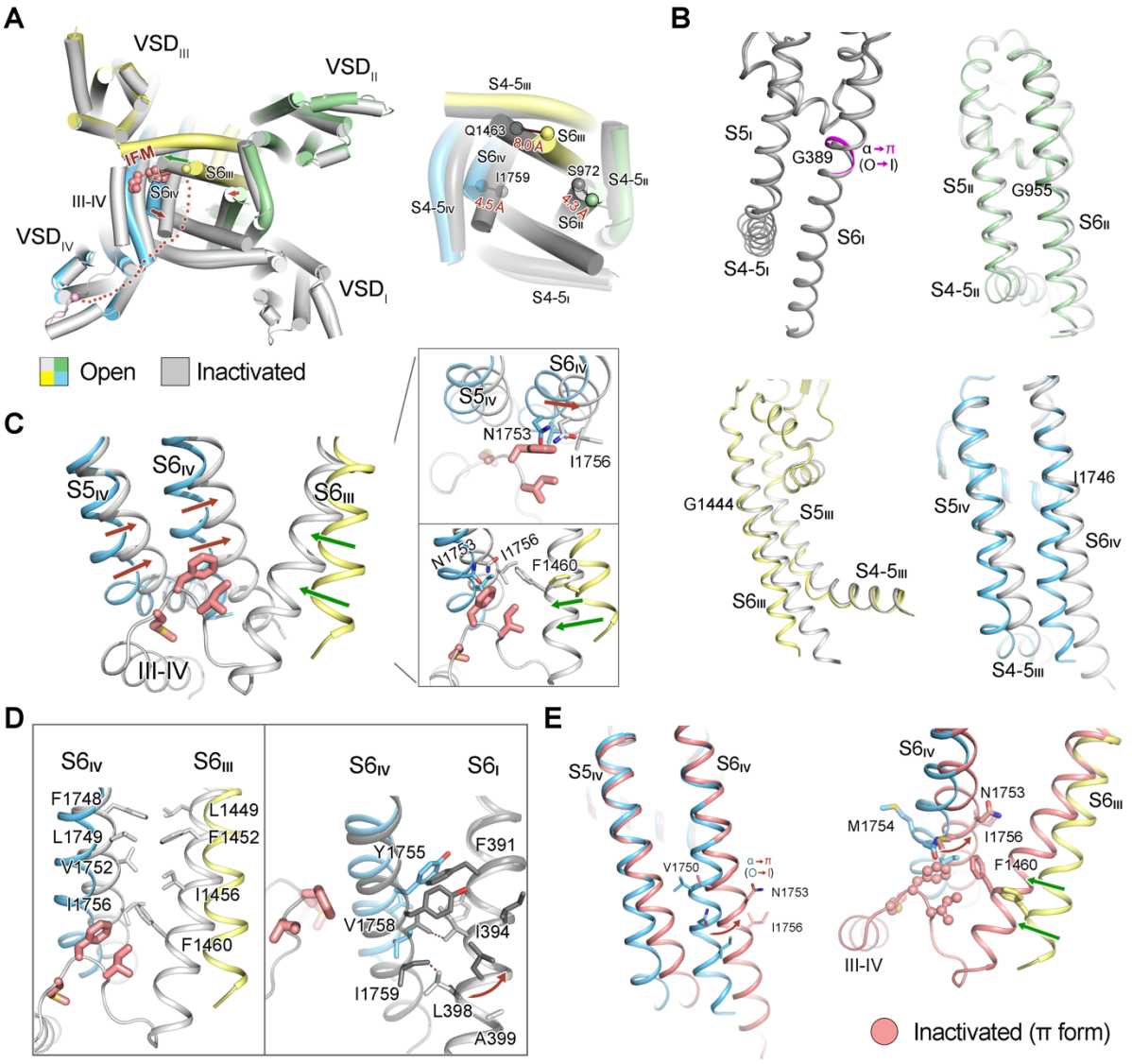

Figure 5 | Structural changes between the open and fast-inactivated $Na_v1.7$. (**A**) Conformational shifts of the pore-forming segments associated with IFM-induced gate closure. In the open $Na_v1.7$ structure, the III-IV linker (indicated by the red dotted line), including the IFM motif, is invisible. Structural superimposition of the open and inactivated (PDB code: 7W9K) $Na_v1.7$ relative to the upper half of the pore domain reveals differential shifts of the S6 and S4-5 segments in the four repeats, as highlighted in the enlarged view on the right. (**B**) The pore-forming segments in the four repeats undergo distinct shifts to various extents upon fast inactivation. Whereas the cytosolic halves of the S6 segments in

repeats II, III, and IV swing to different extents, $S6_I$ has an α→π transition in its middle helical turn. The deviation locus in each S6 segment is labelled. Structures of the open and inactivated $Na_v1.7$ are superimposed as in panel **A**, and the pore-forming segments in the four repeats are displayed the views that best reflect their respective deviations. (**C**) The IFM motif pulls $S6_{III}$ and pushes $S6_{IV}$ to close the intracellular gate. When the hydrophobic IFM motif wedges into the corner between the $S4\text{-}5_{III}$ and $S4\text{-}5_{IV}$ segments, it exerts two opposing forces. On one side, a potential clash between the Phe residue with Ile1756 pushes $S6_{IV}$ toward $S6_I$ (upper inset, brown arrows). On the other side, it pulls $S6_{IV}$ toward $S6_{III}$ (lower inset, green arrows), resulting in the formation of a hydrophobic core between Ile1756 on $S6_{IV}$ with the Ile and Phe residues in the IFM motif and Phe1460 on $S6_{III}$. (**D**) Contraction of the pore domain upon fast inactivation. *Left*: The marked shifts of the $S6_{III}$ and $S6_{IV}$ induce their interface rearrangement. As a result, extensive hydrophobic interactions between $S6_{III}$ and $S6_{IV}$ close the wide cleft in the open pore. *Right*: Displacement of $S6_{IV}$ induces the α→π transition in $S6_I$ to avoid steric clash. Without the rotation following the α→π transition in $S6_I$, residues Ile394 and Leu498 would clash with Val1758 and Ile1759 when $S6_{IV}$ is pushed by the IFM motif. (**E**) The π-helical conformation of $S6_{IV}$ provides a more favorable environment for IFM binding at its receptor site, with the polar residue Asn1753 replaced by the hydrophobic Met1754. If this is the bona-fide fast inactivated conformation, the $S6_{IV}$ segment undergoes both swing and axial rotation during fast inactivation.

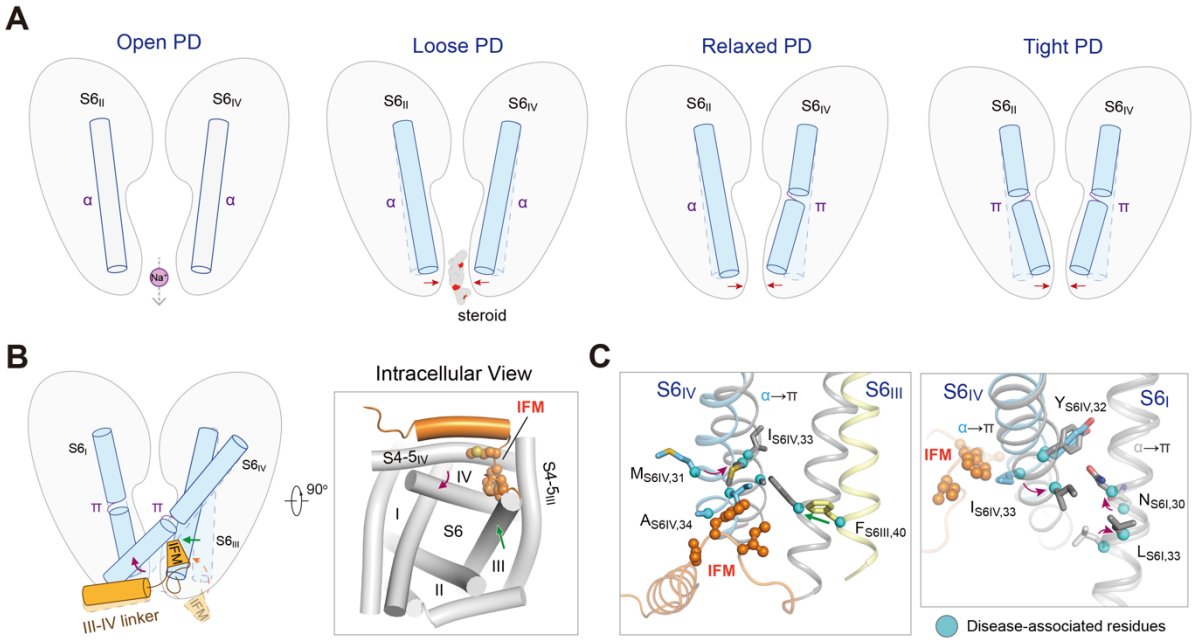

Figure 6 | The 'door wedge' allosteric mechanism governing Na_v channel fast inactivation. (**A**) Schematic overview of the conformational landscape of eukaryotic Na_v pore domains (PDs), spanning open, loose, relaxed, and tight states. These distinct PD architectures are distinguished by differences in the diameter of the intracellular gate and the α- or π-helical conformation of the pore-lining S6 segments. (**B**) Schematic illustration of the 'door wedge' model. During fast inactivation, the IFM motif wedges into its receptor site, pulling $S6_{III}$ and pushing $S6_{IV}$. This movement, accompanied by an α→π transition in the middle turn of $S6_I$ and $S6_{IV}$, cooperatively seals the intracellular gate. (**C**) Disease-associated hotspot residues involved in conformational coupling during fast inactivation. Hotspot Cα atoms are shown as cyan spheres, with example residues highlighted as sticks. Generic-numbered hotspot coupling residues correspond to the following mutations identified across multiple Na_v subtypes, including: Y1781C/$H_{S6IV,32}$, I1782M/$S_{S6IV,33}$ and A1783T/$V_{S6IV,34}$ in $Na_v1.1$-related DRVT; N406K/$S_{S6I,30}$, L409$V_{S6I,33}$, F1473$C_{S6III,40}$, M1766$L_{S6IV,31}$,

Y1767C$_{S6IV,32}$, I1768V$_{S6IV,33}$ in Na$_v$1.5-related LQT3; L407F$_{S6I,33}$ in Na$_v$1.6-related DEE13; and N395K$_{S6I,30}$ and F1460V$_{S6III,40}$ in Na$_v$1.7-related primary erythermalgia.

Materials and Methods

Whole cell electrophysiology

We applied a protocol similar to our previous publication with minor adjustments [47-49]. All currents were recorded in HEK293T cells. Cells were transiently co-transfected with human $Na_v1.7$ and eGFP using lipofectamine 2000 (Invitrogen). Cells with green fluorescence were randomly selected for patch-clamp recordings 24–48 h after transfection. All experiments were performed at room temperature.

Currents were recorded using an EPC10-USB amplifier with Patchmaster software v2*90.2 (HEKA Elektronik), filtered at 3 kHz (low-pass Bessel filter) and sampled at 50 kHz. The borosilicate pipettes (Sutter Instrument) used in all experiments had a resistance of 2-4 MΩ, series resistance was compensated by >75%. The electrodes were filled with the internal solution composed of 105 mM CsF, 40 mM CsCl, 10 mM NaCl, 10 mM EGTA, and 10 mM HEPES, pH adjusted to 7.4 with CsOH. The external solution contained 140 mM NaCl, 4 mM KCl, 1.5 mM $CaCl_2$, 1 mM $MgCl_2$, 10 mM D-glucose, and 10 mM HEPES, pH adjusted to 7.4 with NaOH. The linear component of leaky currents and capacitive transients were subtracted using the P/4 procedure. Only cells with high seal resistance (>1 GΩ) were used. To investigate veratridine's effects on $Na_v1.7$, veratridine was dissolved in dimethyl sulfoxide (DMSO; Sigma) to make a stock solution of 100 mM and stored at –20 °C. Working solutions were freshly prepared and perfused to the recording cell using a multichannel perfusion system (VM8, ALA) for several minutes until the pharmacological

effect reached saturation. Prior to drug application, cells were recorded for 5~15 minutes to establish stable peak current.

To assess the inhibitory effect of veratridine on the peak current, cells were held at -120 mV and depolarized to a test pulse to 0 mV for 50 ms. To investigate the use-dependent effect, a train of 30 pulses (5-ms duration to 0 mV) was applied at 5 Hz from a holding potential of –120 mV. The accumulated tail current at the end of the stimulation was normalized to the amplitude of the first peak current. Concentration–response curves were fitted with: Y = Bottom + (Top – Bottom) / (1 + 10^((LogIC_{50}–X) * Hill Slope)), where IC_{50} or EC_{50} represents the drug concentration that inhibits 50% of the peak current or activates 50% of the tail current, respectively; X is log of the drug concentration; and Hill Slope is the slope factor.

To characterize channel gating properties, voltage-dependent activation was assessed using a protocol consisting of steps from a holding potential of –120 mV to voltages ranging from –90 mV to +80 mV for 50 ms in 5-mV increments. Conductance (G) was calculated as $G = I / (V – V_r)$, where V_r is the reversal potential. Normalized conductance was plotted against the test voltage (from –90 mV to +30 or +40 mV) to generate activation curves. Voltage-dependent steady-state inactivation was determined with a two-pulse protocol, in which cells were conditioned with 1,000-ms pre-pulses from –130 mV (or –150 mV for $Na_v1.7$-L1449A) to 0 mV in 5-mV increments, followed by a 50-ms test pulse to 0 mV. Normalized peak

currents were plotted against pre-pulse voltage to construct inactivation curves. Both activation and inactivation relationships were fitted with a Boltzmann function to determine the $V_{1/2}$ and slope factors (k).

To ensure data integrity, rigorous quality control criteria were applied, excluding activation curves with slope values (k) ≤ 4. Data were processed using Fitmaster (HEKA Elektronik), Igor Pro (WaveMetrics), and GraphPad Prism (GraphPad Software). All quantitative data are presented as mean ± SEM, with n representing the number of independently recorded cells. Statistical significance was assessed using one-way ANOVA and the extra sum-of-squares F test.

Cell culture and transient expression of human $Na_v1.7$ complex in HEK293F cells

The proteins were expressed using the same codon-optimized constructs from our previous work, specifically human $Na_v1.7$ (Uniprot Q15858), β1 subunit (Uniprot Q07699), and β2 subunit (Uniprot O60939) in pCAG expression vector. HEK293F cells (Thermo Fisher Scientific, R79007) were maintained in SMM 293T-II medium (Sino Biological Inc.) at 37 °C under 5% CO_2 and 60% humidity. For transient expression of the human $Na_v1.7$ complex, each liter culture at a density of 1.5–2.0 × 10^6 cells per mL was transfected with a mixture of 2.5 mg plasmids, including 1.5 mg $Na_v1.7$, 0.5 mg β1, and 0.5 mg β2. The plasmid mixture was pre-incubated with 4 mg 40-kDa linear PEI (Polysciences) in 50 ml fresh medium for 15–30 minutes.

Protein purification of human $Na_v1.7$-Veratridine complexes

Transfected HEK293F cells (24 L) were harvested ~48 h post-transfection by centrifugation at 3,600 × *g* for 10 min and resuspended in lysis buffer containing 25 mM Tris-HCl (pH 7.5) and 150 mM NaCl. The suspension was supplemented with 0.1 μM veratridine (MCE), 2 mM PMSF, and protease inhibitor cocktail (Selleckchem), followed by incubation at 4 °C with gentle rotation for 30 min. n-Dodecyl-β-D-maltopyranoside (DDM, Anatrace) was then added to a final concentration of 1% (w/v), along with cholesteryl hemisuccinate Tris salt (CHS, Anatrace) at 0.1% (w/v). The mixture was incubated at 4 °C for an additional 2 h. The supernatant obtained by centrifugation at 16,000 × *g* for 45 min was applied to anti-FLAG M2 affinity resin (Sigma) and incubated for batch binding. The resin was washed four times with wash buffer (buffer W) containing 25 mM Tris-HCl (pH 7.5), 150 mM NaCl, 0.06% GDN, 0.1 μM veratridine, and protease inhibitors. Bound proteins were eluted with buffer W supplemented with 0.2 mg mL^{-1} FLAG peptide (GenScript). The eluent was subsequently passed through Strep-Tactin Sepharose resin (IBA) by gravity flow, washed four times with buffer W, and eluted with buffer W containing 2.5 mM desthiobiotin (IBA). The final eluate was concentrated using a 100-kDa molecular weight cut-off Amicon filter unit (Millipore) and subjected to size-exclusion chromatography on a Superose 6 10/300 GL column (GE Healthcare) pre-equilibrated in buffer containing 25 mM Tris-HCl (pH 7.5), 150 mM NaCl, 0.02% GDN, and 0.1 mM veratridine. The peak fractions were pooled supplemented with 0.5 mM veratridine and incubated at 4 °C for 30 minutes; then concentrated to ~10 mg mL^{-1} for cryo-grid preparation.

Cryo-EM sample preparation and data acquisition

UltrAuFoil (R1.2/1.3 300 mesh, Quantifoil) grids were glow-discharged with easiGlow (PELCO) using 15 mA for 15 s at 0.37 mBar. Vitrobot Mark IV chamber was pre-cooled to 10 °C with 100% humidity. 3 µl concentrated $Na_v1.7$-veratridine was applied to freshly treated grid, which was then blotted with filter paper for 4 s and plunged into liquid ethane cooled by liquid nitrogen. Grids were loaded to a 300 kV Titan Krios G3i with spherical aberration (Cs) image corrector (Thermo Fisher). Micrographs were automated recorded in SerialEM by a Gif Quantum K2 Summit camera (Gatan) with 20 eV slit in super-resolution mode at a nominal magnification of 105,000×, resulting in a calibrated pixel size of 0.557 Å. Each movie stack was exposed for 5.6 s (0.175 s per frame, 32 frames) with a total electron dose of ~ 50 $e^-/Å^2$. The movie stacks were aligned, summed and dose-weighted using Warp and binned to a pixel size of 1.114 Å per pixel.

Data processing

A total of 5,021 micrographs were collected and preprocessed on-the-fly in Warp [50], then imported into cryoSPARC [51]. Particles from 100 micrographs were initially auto-picked using blob picking and subjected to 2D classification to generate templates. Class averages displaying clear features were selected for template-based particle picking for the full dataset and *Ab-initio* reconstruction. Picked and extracted bin4 particles were further cleaned via 2D classification to remove obvious junk. The cleaned dataset was subjected to heterogeneous refinement using two initial references derived from *Ab-initio* reconstruction. Bin2 particles

were re-extracted from selected good class, followed by four rounds of heterogeneous refinement and duplicate removal. The best-resolved class was extracted into bin1 for further processing. The selected particles were subjected to two additional rounds of heterogeneous refinement incorporating higher-resolution features. Subsequent non-uniform (NU) refinement of the dominant class, comprising 631,118 particles, yielded a reconstruction at an overall resolution of 2.7 Å. In this reconstruction, the $S6_{III}$ segment exhibited branched density, suggesting a mixed conformational state. To resolve structural heterogeneity, unsupervised 3D classification was performed on the 631,118 particles without providing multiple manually defined references. A range of different initial resolution filters and class numbers, with "force hard classification" enabled, was tried. Classification with a 6 Å low-pass filter and four output classes successfully resolved three distinct conformational states: the open state, the site I-bound state, and the apo-state. The resulting 3D classes were subsequently used as references for heterogeneous refinement, followed by final round of non-uniform refinement. Final reconstructions were obtained at overall resolutions of 2.9 Å for the open state (133,758 particles, 21.2%), 2.7 Å for the site I-bound state (335,177 particles, 53.1%), and 2.9 Å for the apo state (162,183 particles, 25.7%).

Model building and refinement

The published apo-state structure (PDB: 7w9k) was applied as the initial model for $hNa_v1.7$-veratridine complexes and underwent manual inspection and adjustments in COOT [52]. The veratridine molecules were then modeled and refined based on the density in COOT [52].

Subsequent refinement was performed using the real-space refinement in PHENIX [53], followed by molecular dynamics-based optimization in ISOLDE [54]. A final round of real-space refinement in PHENIX [53] was conducted to complete and validate the model. Validation results are detailed in Table S3.

Molecular dynamics simulations

The protein models were built with our cryo-EM structures of hNav1.7V_O, hNav1.7 apo, and the previously resolved structure rNav1.5-QQQ (PDB: 7FBS) as well as its rebuilt version. Only the pore domains (residue 233-409, 850-977, 1306-1463, and 1629-1769 in $Na_v1.7$, and residue 236-429, 824-945, 1320-1481, and 1644-1777 in $Na_v1.5$) were included in the simulation systems. CHARMM-GUI [55] was used to build the simulation systems. The protein models were embedded into a POPC lipid bilayer. After membrane insertion, the system was solvated in 0.15 M NaCl solution. The simulation box was around $10\times10\times12$ nm^3, which comprised ~120,000 atoms.

We performed MD simulations with GROMACS [56] version 2021.2, using the CHARMM36m force field [57] and CHARMM TIP3P water model. For all the production simulations, the time step was 2 fs. The v-rescale algorithm with a time constant of 0.5 ps was used to maintain the temperature at 310 K [58], and the Parrinello-Rahman algorithm with a time constant of 5 ps was used to maintain the pressure at 1 bar [59]. The Particle-Mesh Ewald method was used to calculate long-range electrostatics with a cut-off of 1.2 nm [60], and the van der Waals

interactions were smoothly switched off from 1.0 nm to 1.2 nm. The bonds involving hydrogen were constrained using the LINCS algorithm [61]. The MDAnalysis package [62] was used to analyze the MD simulation results. PyMOL was used to render molecular visualizations [28]. The default CHARMM-GUI protocol was used to progressively equilibrate the system, including 5000 steps of energy minimization, 250 ps NVT equilibration, and 1625 ps NPT equilibration. Then we restrained the Cα atoms of the protein with a force constant of 1000 kJ/mol/nm^2 to perform another 100 ns NPT equilibration. For production simulations, we relaxed the restraints of pore helix (10 residues before and after the DEKA locus in the SF), while the Cα atoms in other regions were still restrained. We performed ion permeation simulations by applying an electric field of 0.01 V/nm along the pore axis pointing to the intracellular direction, which generated a transmembrane potential of ~120 mV. Three replicates of 1.5 μs simulations were performed for each simulation system.

Water distribution analysis

The water distribution around the intracellular gate was estimated from production simulation trajectories. The origin was assigned as the mean position of the four Cα atoms of DEKA locus and then the pore axis was assigned as the z-axis. By binning the z-axis into 2 Å grid and calculating the number of water molecules around 1 nm of the pore axis, we obtained the water density distribution along z-axis from the following equation:

$$\rho = \frac{N}{V} = \frac{N}{\pi r^2 \Delta z}$$

where ρ is water density, N is the number of water molecules observed in the cylinder layer, V is the volume of the cylinder layer, r(=1 nm) is the radius of the cylinder, Δz(=2 Å) is the grid-spacing. Then the density distribution was normalized by the water density in bulk solution.

Ion permeation analysis

The permeation events were determined by analyzing the z coordinates of ion trajectories: if an ion moved from extracellular side across the membrane to the intracellular side, one permeation event was counted. By counting the number of permeation events, the conductance of the channel for ion (g_{ion}) can be calculated as follows:

$$g_{\mathrm{ion}} = \frac{I}{V} = \frac{N_{\mathrm{p}} Q_{\mathrm{ion}}}{tV} = \frac{N_{\mathrm{p}} Q_{\mathrm{ion}}}{tEL_z}$$

where N_{p} is the observed number of permeation events, Q_{ion} is the charge of the permeating ion, t is the simulation time, V is the transmembrane potential, E is the applied electric field, and L_z is the box size in the z direction. Errors were estimated by the standard deviations of three replicates.

Distribution analysis of permeating ions at the gate

To evaluate the asymmetry of the permeation pathway, we analyzed the spatial distribution of permeant ions around the gate region. This analysis selected ions located between z = -30 and -15 Å and within 10 Å of the pore axis, then projected their coordinates onto the membrane

plane. This 2D x-y distribution was normalized to its maximum value to obtain a relative probability.

Data availability

The data that support this study are available from the corresponding authors upon reasonable request. The cryo-EM maps and corresponding atomic coordinates have been deposited in the Electron Microscopy Data Bank (EMDB) and the Protein Data Bank (PDB).

References:

1 Hille, B. *Ion channels of excitable membranes*. 3rd edn, (Sinauer, 2001).

2 Hodgkin, A. L. & Huxley, A. F. Resting and action potentials in single nerve fibres. *The Journal of physiology* **104**, 176-195 (1945).

3 Huang, J., Pan, X. & Yan, N. Structural biology and molecular pharmacology of voltage-gated ion channels. *Nat Rev Mol Cell Biol* **25**, 904-925 (2024). https://doi.org:10.1038/s41580-024-00763-7

4 Liao, M., Cao, E., Julius, D. & Cheng, Y. Structure of the TRPV1 ion channel determined by electron cryo-microscopy. *Nature* **504**, 107-112 (2013). https://doi.org:10.1038/nature12822

5 Kuhlbrandt, W. Biochemistry. The resolution revolution. *Science* **343**, 1443-1444 (2014). https://doi.org:10.1126/science.1251652

6 Shen, H. *et al.* Structure of a eukaryotic voltage-gated sodium channel at near-atomic resolution. *Science* **355**, eaal4326 (2017). https://doi.org:10.1126/science.aal4326

7 Yan, Z. *et al.* Structure of the Nav1.4-beta1 Complex from Electric Eel. *Cell* **170**, 470-482 e411 (2017). https://doi.org:10.1016/j.cell.2017.06.039

8 Pan, X. *et al.* Structure of the human voltage-gated sodium channel Nav1.4 in complex with beta1. *Science* **362** (2018). https://doi.org:10.1126/science.aau2486

9 Jiang, D. *et al.* Structural basis for voltage-sensor trapping of the cardiac sodium channel by a deathstalker scorpion toxin. *Nat Commun* **12**, 128 (2021). https://doi.org:10.1038/s41467-020-20078-3

10 Clairfeuille, T. *et al.* Structural basis of alpha-scorpion toxin action on Nav channels. *Science* **363** (2019). https://doi.org:10.1126/science.aav8573

11 Jiang, D. *et al.* Open-state structure and pore gating mechanism of the cardiac sodium channel. *Cell* **184**, 5151-5162.e5111 (2021). https://doi.org:10.1016/j.cell.2021.08.021

12 Huang, G. *et al.* Unwinding and spiral sliding of S4 and domain rotation of VSD during the electromechanical coupling in Na(v)1.7. *Proc Natl Acad Sci U S A* **119**, e2209164119 (2022). https://doi.org:10.1073/pnas.2209164119

13 Li, Z. *et al.* Dissection of the structure-function relationship of Na(v) channels. *Proc Natl Acad Sci U S A* **121**, e2322899121 (2024). https://doi.org:10.1073/pnas.2322899121

14 Cox, J. J. *et al.* An SCN9A channelopathy causes congenital inability to experience pain. *Nature* **444**, 894-898 (2006). https://doi.org:10.1038/nature05413

15 Cummins, T. R., Dib-Hajj, S. D. & Waxman, S. G. Electrophysiological properties of mutant Nav1.7 sodium channels in a painful inherited neuropathy. *J Neurosci* **24**, 8232-8236 (2004). https://doi.org:10.1523/JNEUROSCI.2695-04.2004

16 Nassar, M. A. *et al.* Nociceptor-specific gene deletion reveals a major role for Nav1.7 (PN1) in acute and inflammatory pain. *Proc Natl Acad Sci U S A* **101**, 12706-12711 (2004). https://doi.org:10.1073/pnas.0404915101

17 Yang, Y. *et al.* Mutations in SCN9A, encoding a sodium channel alpha subunit, in patients with primary erythermalgia. *Journal of medical genetics* **41**, 171-174 (2004).

18 Shen, H., Liu, D., Wu, K., Lei, J. & Yan, N. Structures of human Nav1.7 channel in complex with auxiliary subunits and animal toxins. *Science* **363**, 1303-1308 (2019). https://doi.org:10.1126/science.aaw2493

19 Huang, G. *et al.* High-resolution structures of human Na(v)1.7 reveal gating modulation through α-π helical transition of S6(IV). *Cell Rep* **39**, 110735 (2022). https://doi.org:10.1016/j.celrep.2022.110735

20 Zhang, J. *et al.* Structural basis for Na(V)1.7 inhibition by pore blockers. *Nat Struct Mol Biol* **29**, 1208-1216 (2022). https://doi.org:10.1038/s41594-022-00860-1

21 Wu, Q. *et al.* Structural mapping of Na(v)1.7 antagonists. *Nat Commun* **14**, 3224 (2023). https://doi.org:10.1038/s41467-023-38942-3

22 Huang, J. *et al.* Cannabidiol inhibits Na(v) channels through two distinct binding sites. *Nat Commun* **14**, 3613 (2023). https://doi.org:10.1038/s41467-023-39307-6

23 Huang, J., Fan, X., Jin, X., Teng, L. & Yan, N. Dual-pocket inhibition of Na(v) channels by the antiepileptic drug lamotrigine. *Proc Natl Acad Sci U S A* **120**, e2309773120 (2023). https://doi.org:10.1073/pnas.2309773120

24 Sutro, J. B. Kinetics of veratridine action on Na channels of skeletal muscle. *J Gen Physiol* **87**, 1-24 (1986). https://doi.org:10.1085/jgp.87.1.1

25 Leibowitz, M. D., Sutro, J. B. & Hille, B. Voltage-dependent gating of veratridine-modified Na channels. *J Gen Physiol* **87**, 25-46 (1986). https://doi.org:10.1085/jgp.87.1.25

26 Ulbricht, W. The effect of veratridine on excitable membranes of nerve and muscle. *Ergeb Physiol* **61**, 18-71 (1969). https://doi.org:10.1007/BFb0111446

27 Zhang, X. Y., Bi, R. Y., Zhang, P. & Gan, Y. H. Veratridine modifies the gating of human voltage-gated sodium channel Nav1.7. *Acta Pharmacol Sin* **39**, 1716-1724 (2018). https://doi.org:10.1038/s41401-018-0065-z

28 DeLano, W. L. The PyMOL Molecular Graphics System. *on World Wide Web http://www.pymol.org* (2002).

29 Fan, X. *et al.* Phrixotoxin-3 binds to three distinct antagonistic sites on human Na(v)1.6. *Cell Res* **35**, 610-613 (2025). https://doi.org:10.1038/s41422-025-01141-4

30 Gao, S. *et al.* Structural basis for human Ca(v)1.2 inhibition by multiple drugs and the neurotoxin calciseptine. *Cell* **186**, 5363-5374.e5316 (2023). https://doi.org:10.1016/j.cell.2023.10.007

31 Jin, X., Huang, J., Wang, H., Wang, K. & Yan, N. A versatile residue numbering scheme for Nav and Cav channels. *Cell Chemical Biology* **31**, 1394-1404 (2024).

32 Weiss, R. E. & Horn, R. Functional differences between two classes of sodium channels in developing rat skeletal muscle. *Science* **233**, 361-364 (1986).

33 Liu, Y., Bassetto, C. A. Z., Jr., Pinto, B. I. & Bezanilla, F. A mechanistic reinterpretation of fast inactivation in voltage-gated Na(+) channels. *Nat Commun* **14**, 5072 (2023). https://doi.org:10.1038/s41467-023-40514-4

34 Wang, G., Dugas, M., Armah, B. I. & Honerjäger, P. Sodium channel comodification with full activator reveals veratridine reaction dynamics. *Molecular pharmacology* **37**, 144-148 (1990).

35 Barnes, S. & Hille, B. Veratridine modifies open sodium channels. *The Journal of general physiology* **91**, 421-443 (1988).

36 Shen, H. *et al.* Structural basis for the modulation of voltage-gated sodium channels by animal toxins. *Science* **362** (2018). https://doi.org:10.1126/science.aau2596

37 Armstrong, C. M., Bezanilla, F. & Rojas, E. Destruction of sodium conductance inactivation in squid axons perfused with pronase. *The Journal of general physiology* **62**, 375-391 (1973).

38 West, J. W. *et al.* A cluster of hydrophobic amino acid residues required for fast Na(+)-channel inactivation. *Proceedings of the National Academy of Sciences of the United States of America* **89**, 10910-10914 (1992).

39 Li, Z. *et al.* Structure of human Na_v1.5 reveals the fast inactivation-related segments as a mutational hotspot for the long QT syndrome. *Proceedings of the National Academy of Sciences* **118** (2021).

40 Li, Z. *et al.* Quinidine-bound human Nav1.5 structure reveals a mutational hotspot for Long QT Syndrome mapped to inactivation-related segments *Submitted* (2020).

41 Hu, R.-M. *et al.* Mexiletine rescues a mixed biophysical phenotype of the cardiac sodium channel arising from the SCN5A mutation, N406K, found in LQT3 patients. *Channels* **12**, 176-186 (2018).

42 Itoh, H., Shimizu, M., Takata, S., Mabuchi, H. & Imoto, K. A novel missense mutation in the SCN5A gene associated with Brugada syndrome bidirectionally affecting blocking actions of antiarrhythmic drugs. *Journal of cardiovascular electrophysiology* **16**, 486-493 (2005).

43 Huang, H., Priori, S. G., Napolitano, C., O'Leary, M. E. & Chahine, M. Y1767C, a novel SCN5A mutation, induces a persistent Na+ current and potentiates ranolazine inhibition of Nav1. 5 channels. *American Journal of Physiology-Heart and Circulatory Physiology* **300**, H288-H299 (2011).

44 Clancy, C. E., Tateyama, M., Liu, H., Wehrens, X. H. & Kass, R. S. Non-equilibrium gating in cardiac Na+ channels: an original mechanism of arrhythmia. *Circulation* **107**, 2233-2237 (2003).

45 Meng, E. C., Pettersen, E. F., Couch, G. S., Huang, C. C. & Ferrin, T. E. Tools for integrated sequence-structure analysis with UCSF Chimera. *BMC Bioinformatics* **7**, 339 (2006). https://doi.org:10.1186/1471-2105-7-339

46 Smart, O. S., Neduvelil, J. G., Wang, X., Wallace, B. A. & Sansom, M. S. HOLE: a program for the analysis of the pore dimensions of ion channel structural models. *J Mol Graph* **14**, 354-360, 376 (1996). https://doi.org:10.1016/s0263-7855(97)00009-x

47 Li, Z. *et al.* Structure of human Na(v)1.5 reveals the fast inactivation-related segments as a mutational hotspot for the long QT syndrome. *Proc Natl Acad Sci U S A* **118** (2021). https://doi.org:10.1073/pnas.2100069118

48 Huang, X. *et al.* Structural basis for high-voltage activation and subtype-specific inhibition of human Na(v)1.8. *Proc Natl Acad Sci U S A* **119**, e2208211119 (2022). https://doi.org:10.1073/pnas.2208211119

49 Fan, X., Huang, J., Jin, X. & Yan, N. Cryo-EM structure of human voltage-gated sodium channel Na(v)1.6. *Proc Natl Acad Sci U S A* **120**, e2220578120 (2023). https://doi.org:10.1073/pnas.2220578120

50 Tegunov, D. & Cramer, P. Real-time cryo-electron microscopy data preprocessing with Warp. *Nat Methods* **16**, 1146-1152 (2019). https://doi.org:10.1038/s41592-019-0580-y

51 Punjani, A., Rubinstein, J. L., Fleet, D. J. & Brubaker, M. A. cryoSPARC: algorithms for rapid unsupervised cryo-EM structure determination. *Nat Methods* **14**, 290-296 (2017). https://doi.org:10.1038/nmeth.4169

52 Emsley, P., Lohkamp, B., Scott, W. G. & Cowtan, K. Features and development of Coot. *Acta Crystallogr D Biol Crystallogr* **66**, 486-501 (2010). https://doi.org:10.1107/S0907444910007493

53 Afonine, P. V. *et al.* Towards automated crystallographic structure refinement with phenix.refine. *Acta Crystallogr D Biol Crystallogr* **68**, 352-367 (2012). https://doi.org:10.1107/S0907444912001308

54 Croll, T. I. ISOLDE: a physically realistic environment for model building into low-resolution electron-density maps. *Acta Crystallogr D Struct Biol* **74**, 519-530 (2018). https://doi.org:10.1107/S2059798318002425

55 Jo, S., Kim, T., Iyer, V. G. & Im, W. CHARMM-GUI: A web-based graphical user interface for CHARMM. *Journal of Computational Chemistry* **29**, 1859-1865 (2008). https://doi.org:https://doi.org/10.1002/jcc.20945

56 Abraham, M. J. *et al.* GROMACS: High performance molecular simulations through multi-level parallelism from laptops to supercomputers. *SoftwareX* **1-2**, 19-25 (2015). https://doi.org:https://doi.org/10.1016/j.softx.2015.06.001

57 Huang, J. *et al.* CHARMM36m: an improved force field for folded and intrinsically disordered proteins. *Nature Methods* **14**, 71-73 (2017). https://doi.org:10.1038/nmeth.4067

58 Bussi, G., Donadio, D. & Parrinello, M. Canonical sampling through velocity rescaling. *The Journal of chemical physics* **126**, 014101 (2007). https://doi.org:10.1063/1.2408420

59 Parrinello, M. & Rahman, A. Polymorphic transitions in single crystals: A new molecular dynamics method. *Journal of Applied Physics* **52**, 7182-7190 (1981). https://doi.org:10.1063/1.328693

60 Darden, T., York, D. & Pedersen, L. Particle mesh Ewald: An N·log(N) method for Ewald sums in large systems. *The Journal of chemical physics* **98**, 10089-10092 (1993). https://doi.org:10.1063/1.464397

61 Hess, B., Bekker, H., Berendsen, H. J. C. & Fraaije, J. G. E. M. LINCS: A linear constraint solver for molecular simulations. *Journal of Computational Chemistry* **18**, 1463-1472 (1997). https://doi.org:https://doi.org/10.1002/(SICI)1096-987X(199709)18:12<1463::AID-JCC4>3.0.CO;2-H

62 Michaud-Agrawal, N., Denning, E. J., Woolf, T. B. & Beckstein, O. MDAnalysis: A toolkit for the analysis of molecular dynamics simulations. *Journal of Computational Chemistry* **32**, 2319-2327 (2011). https://doi.org:https://doi.org/10.1002/jcc.21787